Available online at www.sciencedirect.com
SCIENCE DIRECT®
ELSEVIER
International Journal of Multiphase Flow 30 (2004) 107–124
International Journal of Multiphase Flow
www.elsevier.com/locate/ijmulflow

Interfacial measurements in stratified types of flow. Part I: New optical measurement technique and dry angle measurements

Thierry Ursenbacher, Leszek Wojtan, John R. Thome *

Laboratory of Heat and Mass Transfer (LTCM), Faculty of Engineering Science (STE), Swiss Federal Institute of Technology Lausanne (EPFL), CH-1015 Lausanne, Switzerland

Received 20 January 2003; received in revised form 24 November 2003

Abstract

The development of a new non-intrusive computerized image analysis and optical observation method for accurately detecting the vapor–liquid interface in stratified two-phase flows is presented. This technique is applied to a round horizontal sight glass tube using a monochromatic laser sheet for observing two-phase flow patterns and for measuring cross-sectional dry angles and void fractions in these types of flow. The cross-sectional image observed externally is distorted by refraction and is thus reconstructed by computer. From this image, the shape of the vapor–liquid interface is detected and the dry angle and void fraction are accurately determinable over a wide range of conditions for a glass tube of 13.6 mm diameter. Results for dry angle are reported here while the test facility and void fraction measurements are presented in Part II. R-22 and R-410A are the test fluids. Dry angles were quite close to values predicted for stratified flow and much larger than comparable values for air–water flows.

Keywords: Void fraction; Two-phase flows; Flow boiling; Stratified flows; Wavy flows; Liquid–vapor interface; Free surface detection; Dry angle

1. Introduction

The development of the flow pattern/flow structure based, boiling heat transfer model of Kattan et al. (1998a,b,c) resulted in a notable improvement in the accuracy of two-phase flow heat

* Corresponding author. Tel.: +41-21-693-5981; fax: +41-21-693-5960.
E-mail address: john.thome@epfl.ch (J.R. Thome).

0301-9322/$ - see front matter
doi:10.1016/j.ijmultiphaseflow.2003.11.010

transfer predictions. Prior methods were not reliable because they did not consider different two-phase flow regimes and were especially weak at high vapor qualities and for stratified types of flows. Similarly, an analogous flow pattern based heat transfer model has been proposed for condensation by Thome et al. (2003) with similar benefits. Currently, two-phase heat transfer prediction models, which account for flow regime effects, are considered state of the art. Further development of these models requires precise prediction of flow pattern transition, mean phase velocities, dry angles and liquid film thickness. The most important parameter influencing these flow characteristics is the cross-sectional void fraction ε, which is defined as the ratio of the cross-sectional area occupied by the vapor phase to the total cross-sectional area of the channel. For stratified flows, the dry angle is equally important because it delineates the wet and dry perimeters for heat transfer. Part I describes a new measurement technique for interfacial measurements and presents dry angle results and Part II presents dynamic cross-sectional void fractions measurements. The tests were run with two refrigerants (R-22 and R-410A) over a wide range of test conditions.

According to the simplified flow structures assumed to represent annular, stratified-wavy and stratified flows as annular films (Fig. 1), Kattan et al. use the cross-sectional void fraction ε and dry angle θ_{dry} in their flow boiling heat transfer model for evaporation in horizontal tubes:

$$\alpha_{tp} = \frac{\theta_{dry}\alpha_{dry} + (2\pi - \theta_{dry})(\alpha_{nb}^3 + \alpha_{cb}^3)^{1/3}}{2\pi} \tag{1}$$

where α_{tp} is the perimeter averaged two-phase heat transfer coefficient, α_{nb} is the nucleate boiling heat transfer coefficient, α_{cb} is the convective boiling heat transfer coefficient and α_{dry} is the vapor heat transfer coefficient.

Thus, both dry angle and void fraction are important parameters affecting heat transfer in flow boiling and have a similar importance to condensation and two-phase pressure drops. Since most

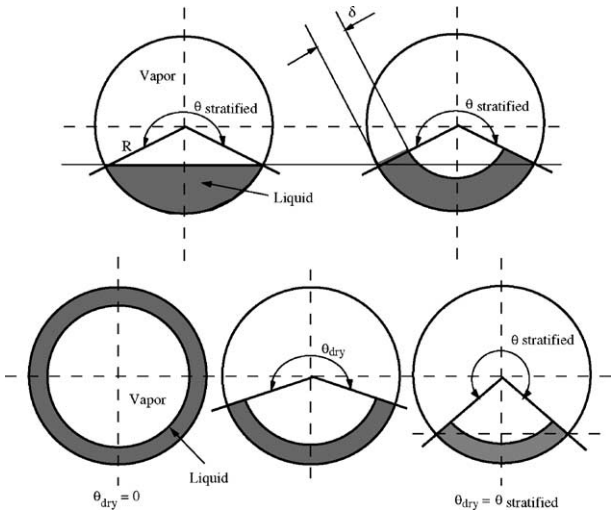

Fig. 1. Flow structures for annular, stratified-wavy and fully stratified flows (left to right in the bottom three diagrams) and for fully stratified flow and its film flow equivalent (top two diagrams).

measurements in the literature are for water (a high surface tension, large contact angle fluid) with air, they are not representative of two-phase flows of low surface tension/low contact angle fluids, which encompasses most refrigerants and light hydrocarbons. Thus the present test fluids are R-22 and R-410A.

In the present study, a new optical image analysis technique utilizing a laser sheet and a video camera to determine the two-phase interface inside round horizontal glass tubes is presented. The technique is only applicable to stratified two-phase flows, in particular: fully stratified flow, stratified-wavy flow and annular flow with partial dryout around at least the top half of the tube. Slug flows have also been successfully measured. Since the void fraction is determined from the locus of the interface, the void fraction is only determinable if no bubbles are in the liquid phase. Hence, test results are only reported for conditions in which no bubbles are visible. Using a higher resolution digital video camera than presently used in the future it is also contemplated to make detailed measurements of the interfacial roughness.

The objective here is to develop a technique that is appropriate for measuring void fractions for these types of flows in tubular sight glasses located at the end of heat transfer test sections. This will allow observation of flow patterns and measurement of dry angles, void fractions, heat transfer coefficients and two-phase pressure drops in a single test facility for experimental studies on in-tube boiling and condensation.

Numerous methods have been developed over the years for measuring cross-sectional void fraction in two-phase flows: resistance sensors (Krepper et al., 1999), capacitance or conductance sensors (Costigan and Whalley, 1996), refractive fiber optic probes (Cartellier, 1996), radiation attenuation techniques (Kendoush and Sarkis, 2002), ultrasonic tomography (Xu and Xu, 1997), etc. With intrusive methods, all types of sensors or probes disturb to some extent the flow field and induce imperfect identification of the interface between the gas and liquid. Non-intrusive methods, such as radiation techniques and conductance measurements, yield mean void fraction values of the cross-section. Using these methods, one cannot determine either the dry angle nor the shape of the interface between the gas and liquid. More sophisticated non-intrusive methods, such as real time neutron radiography (RTNR) and X-ray computed tomography (X-CT), allow for the measurement of the distribution of void fraction. Notably, the results obtained by Harvel et al. (1999) show reconstruction of two-dimensional cross-sectional images taken at frequencies up to 250 Hz, for instance. Harvel also used a RTNR technique to determine lateral void fraction with respect to time. The accuracy of these methods is not reported in the literature. Also, both techniques require radiation protection systems that preclude their general use.

2. Measurement strategy

As has been mentioned in the introduction, the main objective of the new optical technique is to measure cross-sectional void fraction by determination of the ratio of area occupied by gas to the total area of the channel and the dry angle of the upper tube perimeter. For this purpose, a borosilicate glass tube has been installed at the end of the heat transfer measurement test section. The external diameter of the glass tube is 16 mm and the wall thickness is 1.2 mm (with a very uniform thickness and roundness, i.e. ± 0.02 mm). Before installation, the glass tube was tested up to an internal pressure of 5 MPa (one-half of its maximum recommended working pressure). The

optical set-up scheme is presented in Fig. 2. A perpendicular cross-section of the glass tube and fluid within are illuminated by a laser sheet (Spectra Physics laser Millennia II), and the images are recorded by a digital camera (Panasonic CCD camera type GP-LM7/TA) located above the glass tube with a vision angle of 40° with respect to the axis of the tube. The laser sheet is about 0.5 mm thick. The wavelength emitted by the laser is 532 nm and interlaced images are recorded on a Pentium3 PC through a Targa Video card.

The recorded image, representing a cross-sectional view of the two-phase flow, is distorted by the refraction of the light through the internal and external surfaces of the glass. Thus for void fraction measurements to be made, this technique requires reconstruction of the field of the vision to obtain a non-deformed, orthogonal view of the illuminated cross-section. This reconstruction is based on the optical distortion of a regular grid placed inside the glass tube in the same plane as the laser sheet during preliminary tests without any liquid in the tube. The process consists of extracting an inverse transformation function, which is applied to the distorted grid image in order to obtain an image of a regular grid (see next paragraph). This function is then applied to the video images of the two-phase refrigerant flowing in the tube. The transformation, however, is only valid for the cross-sectional fraction occupied by a gas under the condition that the gas-phase is in direct contact with the upper wall of the tube. Therefore, for a fully annular flow the optical deformation of the gas area no longer corresponds to the one on the grid. The presence of a liquid film on the upper wall induces a new deformation of the image depending on the refractive index of the liquid. For this reason, the new technique is only applicable to stratified types of flow without entrained bubbles. Furthermore, the transformation is only valid in the gas phase above the vapor–liquid interface and not below into the liquid phase (where the light is again refracted). Finally, the locus of the interface is detected using image processing, giving the ratio of the area occupied by the vapor phase with the total cross-sectional area, i.e. the instantaneous void fraction as a function of time and the dry angle.

A grid is printed on a glossy paper and fixed on a stopper introduced inside the glass tube in a calibration set-up (Fig. 3) identical to that on the flow boiling test facility (±0.01 mm for the machined pieces and both tubes have a diameter of 13.60 ± 0.02 mm). The grid is used to model the optical distortion and to calibrate the interface detection procedure between the gas and liquid (see Section 4). Once the optical alignment of the laser and the camera setup are made, it remains

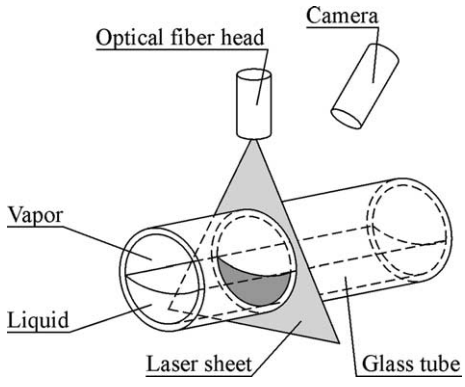

Fig. 2. Schematic of the optical setup.

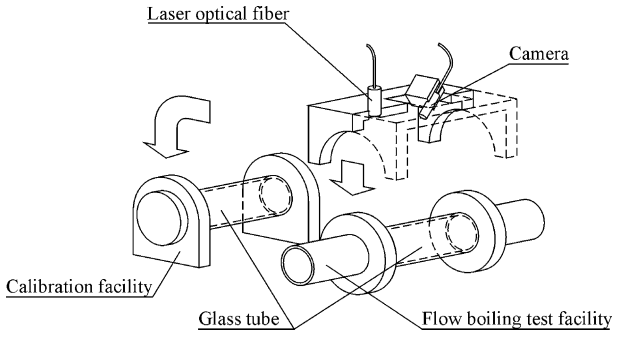

Fig. 3. Image calibration and video acquisition system setups.

unchanged whether the upper support is mounted on the calibration set-up or on the flow boiling test facility. Assurance is made that the upper support structure is precisely horizontal.

The image processing program is coded with LabView (version 6i). This particular language provides a powerful visual interface to the user (graphic and image) allowing a continuous interaction on processing the image.

3. Transformation of distorted images

3.1. Detection of the distorted grid

The distorted grid image is converted into an 8-bits encoded image with 256 levels of grey. Due to the small distance between the camera and the grid (about 3 cm) and the vision angle of 40°, the depth of focus is weak, making it impossible to obtain a well-focused image on the total surface of the grid. The focal plane is thus adjusted on the horizontal grid axis in such a way that the lines above and below the axis do not become too blurred. The zones outside of the grid are eliminated by limiting the image size (from 720×576 pixels to 430×370 pixels) and by adding an elliptical mask to focus only on the internal surface of the glass tube (Fig. 4). Before adding the mask, the image is inverted (in terms of gray levels) allowing an easier distinction of the grid border. In this way, a black line appears as a white one and vice versa. Optically, two types of distortion can be distinguished on the deformed grid image: the bottom part of the grid (under the axis) is vertically compressed (diminution of the space between the horizontal lines) and the upper part is horizontally elongated (increasing space between the vertical lines).

To model the optical deformation, each grid line (vertical and horizontal), must be individually detected. This detection is based on the grey level signal evolution over each pixel row and each pixel column of the image. This signal depends directly both on the line spacing and the line thickness. Numerous grids were thus tested and the choice of a grid having a line spacing of 0.35 mm (i.e. 37 vertical and 37 horizontal lines) and a line thickness of 0.12 mm (0.35 point) was selected. Fig. 5 illustrates the variation in the light signal intensity along the 230th pixel row (1 mm above the grid centerline axis). At each extremity the signal is equal to zero, which corresponds to the presence of the mask (black zone). In the center, the signal evolves in a sinusoidal way: each

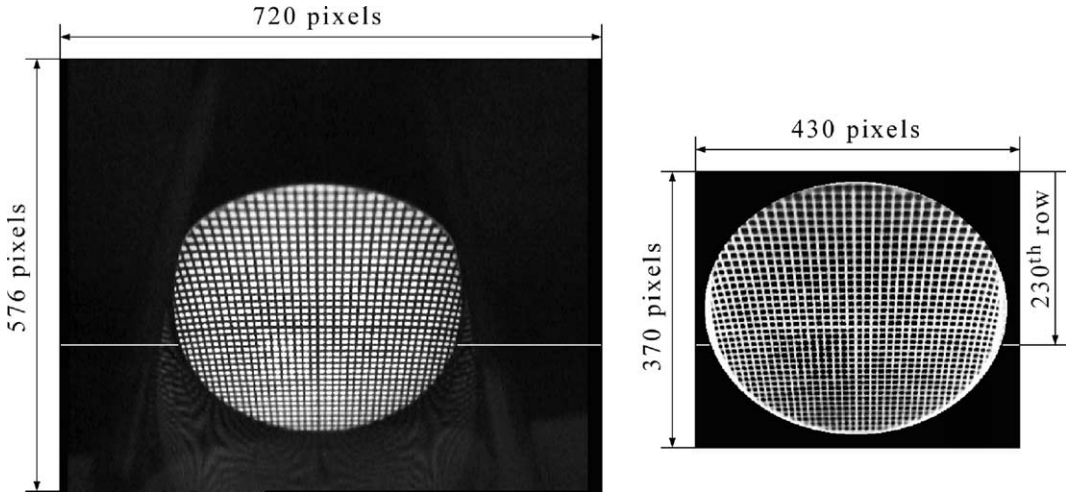

Fig. 4. Original (left) and limited (right) grid image (the white transversal line corresponds to the 230th line, counted from the top on the limited image).

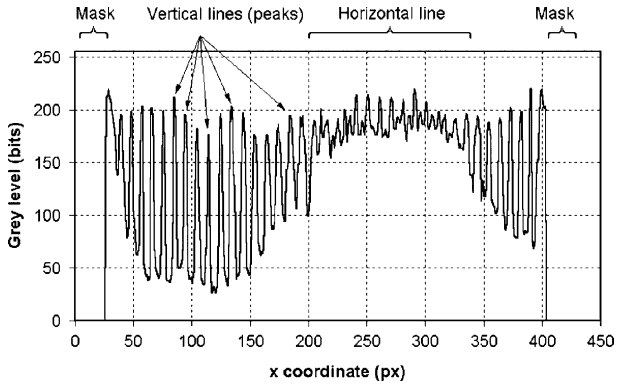

Fig. 5. Evolution of the grey level intensity along the 230th row of pixels (1 mm below the horizontal centerline axis of the grid).

peak corresponds to a vertical line of the grid cut almost perpendicularly by the current pixel row. Therefore by detecting a peak position, one detects a local point of a grid line. Proceeding in this way on each pixel row/column, a collection of spatial points is obtained, which describes all the grid lines. The points of each line are sorted both by proximity and on the a priori knowledge of the spatial shape of each line (mainly vertical or mainly horizontal). Qualitatively, the peak thickness is proportional to the line thickness. With the current grid, the peak thickness is between 3 and 5 pixels wide. Concerning the grid mesh size (line spacing), it fixes the spatial frequency of the signal. A finer size than the one used would risk affecting the difference between the neighboring maximum and minimum values in the grey level signal evolution (i.e. diminution of the sinusoidal amplitude); exaggerating, it means that two successive lines would not be distinguished from each other. Another particular case illustrated in Fig. 5, is where a section of the pixel row of

the image falls directly on a horizontal line of the grid; in this section, the signal is dominated by the white color of the grid line, yielding small differences between the neighboring maximum and minimum values, and thus does not allow one to distinguish the vertical lines. This implies the introduction of an amplitude threshold, which fixes the limit difference between a successive maximum and minimum value (experimentally fixed at 40 bits) and below which the peak is ignored.

Concerning the detection of the position of a peak, the techniques used in the field of DPIV (digital particle image velocimetry) for the detection of the correlation peak are used. Thus, according to Westerweel (1997), if the position of the peak is known a priori only up to 1 pixel resolution, the use of the Gaussian interpolation functions on the first neighbors of a peak allow the estimation of the peak center to approximately ±0.1 pixel. The extraction of the points describing the different lines can be difficult at the perimeter of the grid (the lower differences between the neighboring maximum and the minimum values for $25 < x < 50$ as in Fig. 5) and in the bottom part of the grid (small distance between lines due to optical compression as in Fig. 4).

In order to maintain a high quality in modeling the distortion, a simulation of the camera vision field has been made. This simulation is based on several hypotheses. First, the refraction of an optical beam passing from one medium to another is perfectly described by the law of sines (Descartes law):

$$n_1 \sin i_1 = n_2 \sin i_2 \tag{2}$$

where n_1 and n_2 are the respective refraction indices of the first and second medium, i_1 is the incident angle and i_2 is the refracted angle respectively to the normal component of the plane. Second, the digital camera is represented by a table of pixels (having an equivalent or superior size than the effective CCD cell) and is equipped only with a spherical convergent lens. Furthermore, the path of the light beam is not considered as going from its source point (on the grid) to the receptor (a pixel), but in the inverse direction. Thus, there are two changes in the medium: from air to glass and then from glass to refrigerant vapor. The result of such a simulation is represented in Fig. 6 and is called a *synthetic grid*. The resemblance between the real distorted grid and the synthetic distortion is evident: there is a convergence of the horizontal lines below the centerline axis and a divergence of vertical lines in the upper half.

Next, the information from both grids is coupled comparing the coordinates of each intersection point with respect to the vertical and horizontal symmetry axis. Isolating the evolution of x-coordinates on a horizontal line and the evolution of y-coordinates on a vertical line, the

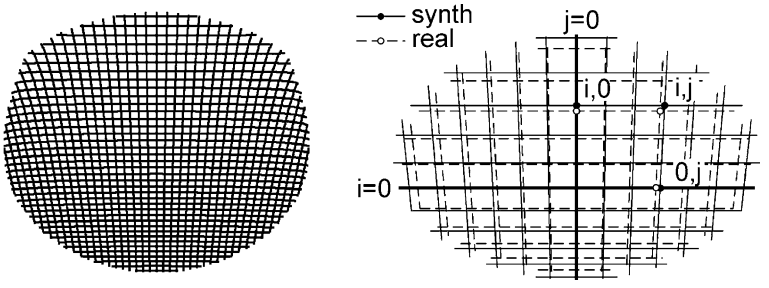

Fig. 6. Synthetic grid (on the left) and coordinate system (on the right).

relationship between the real and the synthetic grid can be described by a second order polynomial function. Now, defining i as the horizontal line index and j as the vertical line index, one obtains:

$$\left(x_{\text{synth } i,j} - x_{\text{synth } i,0}\right) \cdot \left[a_0(i) + a_1(i)j + a_2(i)j^2\right] = x_{\text{real } i,j} - x_{\text{real } i,0} \tag{3}$$

$$\left(y_{\text{synth } i,j} - y_{\text{synth } 0,j}\right) \cdot \left[a_0(j) + a_1(j)i + a_2(j)i^2\right] = y_{\text{real } i,j} - y_{\text{real } 0,j} \tag{4}$$

where for example, $x_{\text{real } i,0}$ is the x-coordinate of the intersection point formed by the ith horizontal line crossing the vertical symmetry axis (line $j = 0$). The coordinates x_{real} and y_{real} refer to the real image but they are measured values as previously described. The variables set $a_k(i)$ where $k = 1, 2$ and 3 corresponds to each horizontal line i, and respectively, each vertical line j has a variables set $a_k(j)$. These variables are extracted by linear regression using a least squares fit. The parameters $a_k(i)$ and $a_k(j)$ are thus coupled by tracing the evolution of these variable sets as functions of the horizontal line index, respectively of the vertical line's index. Referring to Fig. 7, it can be stated that each of the three parameters $a_k(i)$ can be approximated by a first order polynomial function over most of its range. For index values inferior to −10 and greater than +10 (i.e. for the 8 first and 8 last horizontal lines), the real/synthetic comparison shows a clearly different behavior. This results directly from the difficulty to detect the lines close to the grid circumference, which was noted previously above. Using a linear regression in the least squares sense with a Gaussian weight function (where the width parameter is fixed at 8 to attenuate the extremity influence), we obtain for each parameter $a_k(i)$ and $a_k(j)$ a continuous function to describe the geometrical difference between the synthetic and the real grids. From these parameters, the real coordinates of the intersection points can be re-estimated using Eqs. (3) and (4). This approach acts like a smoothing function without losing the original information and generates a spatial distribution function of intersection points without any inflexion point. The vertical and horizontal lines can thus be described mathematically through new intersection points with cubic spline functions. The result of these successive operations is illustrated in Fig. 8. The lines generated from these cubic spline functions correspond closely to the image of the distorted grid.

As previously noted, the maximum geometrical difference between the glass tube used in the calibration set-up and the glass tube in flow boiling test facility is on the order of 0.02 mm. Using the simulation and applying it to a tube with an internal and external diameter of 13.58 and 16.02

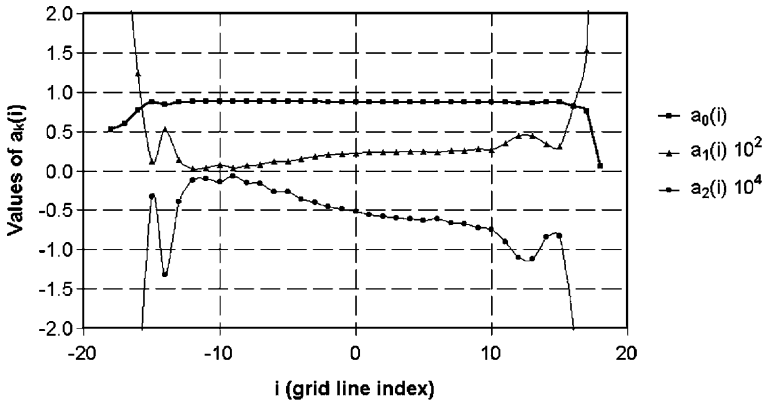

Fig. 7. "Synthetic-to-real" grid coupling parameters as function of grid line index i.

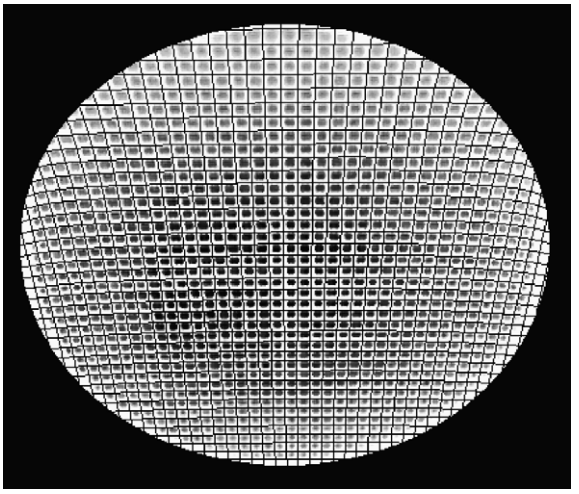

Fig. 8. Cubic spline functions based on intersection points describing horizontal and vertical grid lines.

mm, respectively (instead of 13.60 and 16.00 mm), the maximum difference in terms of coordinates is less than 0.01 mm (i.e. less than 0.4 pixel on the image, which is less than the resolution). This confirms that both the glass tube used for calibration and that on the flow boiling facility can be considered identical.

3.2. Image mapping

The transformation of the distorted grid image into one with parallel vertical and horizontal lines is performed in two distinct steps. This first consists of mapping of the points (each point from the distorted space should correspond to a point on the transformed one). The second phase is the reconstruction of the image itself (reconstruction pixel-by-pixel of the grey level signal from the distorted image with respect to the mapping).

For the first step, the technique consists in associating the intersection points of the deformed grid to the intersection points of the regular grid, which should have the characteristic $y_{\text{transf}} = \text{constant}$ on each horizontal line and $x_{\text{transf}} = \text{constant}$ on each vertical line. To simplify, the transformed grid lines are positioned in a way that the coordinates of their intersection points are expressed as integer values (in order to correspond directly to the pixel coordinates). The choice of these coordinates is such that the global size of the transformed image is the same as the original one. In this way, magnification of the image is avoided, which would amplify any defects (for example, crystalline imperfections in the glass tube). Shrinkage of the image, which would reduce the resolution in the void fraction measurement, is also avoided. Having fixed the vertical and horizontal coordinates of the transformed grid along with knowledge of the real size of the grid line spacing yields the conversion ratio in pixel/mm. The pixel size of a circular mask corresponding to the internal tube diameter can thus be directly deduced and added to the transformed image.

Based on these considerations, the grid is artificially refined to a higher density such that the new grid lines (vertical and horizontal) correspond in size to the pixel grid of the transformed

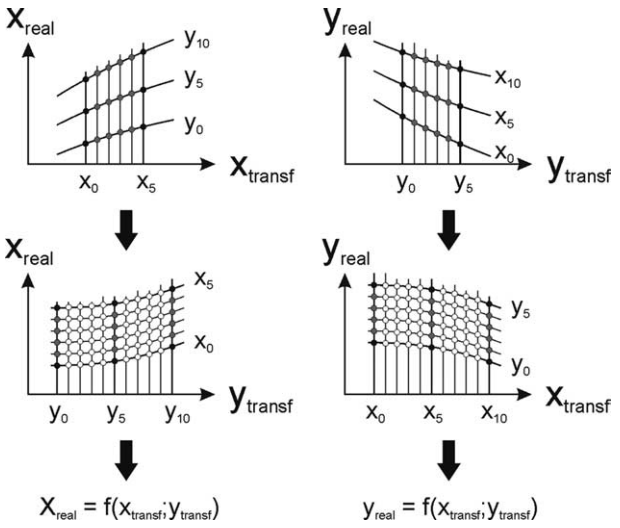

Fig. 9. Mapping of the coordinates.

image (the grey level of each pixel can now be determined). Hence, consider the x-coordinates of the intersection points on the distorted lines as a function of the associated x-coordinates of the intersection points on the regular grid. For each horizontal line, a cubic spline function can be constructed. For each intermediate integer value of x_{transf} (i.e. for each pixel), this allows estimation of the corresponding value x_{real} (Fig. 9). In this way, the number of vertical lines is increased. Consider now the same coordinates x_{real}, but as a function of y_{transf} coordinates. New cubic spline functions can be constructed for each vertical line, which for each integer value of y_{transf} allows the estimation of a value x_{real} on the deformed image. This is the number of horizontal lines, which is increased. Thus, each coordinate couple $(x_{\text{transf}}; y_{\text{transf}})$ is associated to an x_{real} value. Proceeding in a similar way for the coordinates y_{real}, it is possible to associate each pixel $(x_{\text{transf}}; y_{\text{transf}})$ to a corresponding y_{real} value.

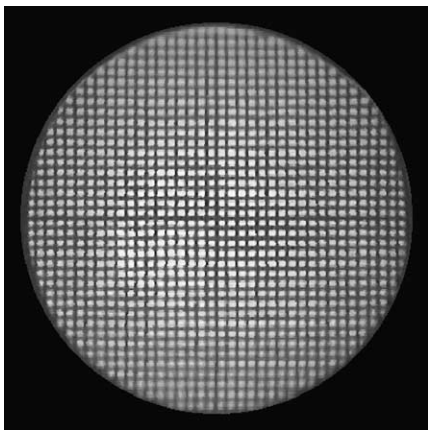

Fig. 10. Transformed grid image.

Finally, each pixel $(x_{transf}; y_{transf})$ receives the intensity of the distorted image pixel containing the corresponding point $(x_{real}; y_{real})$, which are not integer values. More sophisticated techniques have been tested, such as the weighted surface mapping technique proposed by Huang et al. (1993), without improving accuracy. This technique is the fastest, and taking into account the large number of images to process (227'000 in Part II), this approach is the most convenient.

The result of this new operation is illustrated in Fig. 10. Looking in the plane of the drawing, the horizontal and vertical lines in the transformed grid image are nearly perfectly straight and parallel to one another, even near the perimeter.

4. Vapor–liquid interface detection technique

To detect the vapor–liquid interface, two problems need to be resolved. The first one concerns the optical highlighting of the interface (in the visible domain) and the second one is the strategy to systematically detect this interface with image processing.

4.1. Interface highlighting

As specified in Section 2, a laser sheet is used to illuminate the cross-section of the two-phase fluid flowing in the tube. Due to the transparency of the refrigerants tested (R-22 and R-410A), the laser light is neither absorbed by the vapor phase nor the liquid phase and there is no luminescence in the cross-section. Therefore, the presence of a fluorescent in the liquid phase is required to obtain a satisfactory illumination effect. The term luminescence refers to the light emitted by molecules when returning from an electronically excited state to the ground state. In our case, the excited state is produced by the laser light with a wavelength of 532 nm. The excited state of a molecule decays to the ground state under emission of light typically within 0.1–20 ns. Because the period of time during which a molecule remains in its excited state is relatively long, numerous interactions with other species can occur within its lifetime. These include vibrational relaxation and re-orientation in the dielectric field of the solvent, both causing energy to be partially lost. As a result, the luminescence of all organic molecules occurs at longer (less energetic) wavelengths than excitation.

For our tests, rhodamineB (produced by Fluka) was chosen as the fluorescent powder. This fluorescent, when brought to an excited state by the laser light, emits a wavelength of about 627 nm for a maximum absorption at 554 nm. The refrigerant properties are not to be influenced by the trace presence of the fluorescent powder and thus only a trace amount of rhodamineB is added to the refrigerant. This in turn means that the minimum sufficient concentration of the fluorescent for the image processing procedure has to be determined. Both the calibration set-up (static tests) and the flow boiling facility (dynamic tests) were initially used to fix this concentration, but dynamic tests proved to be essential because the fluorescent molecules are excited for a shorter time period than in a static conditions (the excitation duration is the time for the molecules to flow across the laser sheet) and, secondly, the concentration in the flow boiling test facility is not constant (due to partial evaporation of the liquid in the test section and the consequent concentrating of rhodamineB in the remaining liquid by a factor up to 20 times). Based on trials with different amounts of fluorescent powder, the minimum concentration was found to be about 1

molecule of rhodamineB per 100 million molecules of refrigerant and its potential influence on the refrigerant properties was tested during the calibration procedure (described in next section).

Concerning the experimental setup during the tests, many rays of the laser sheet were reflected by the tube. Moreover, the dynamic tests include a flow induced small scale roughness at the vapor–liquid interface, which produced overexposed images due to the laser light reflections. To reduce the negative effect of excess reflections, an optical filter is directly fixed on the CCD camera. This optical filter is a combination of six filters especially used for eye-protection glasses for working with Nd:Yag lasers (in terms of optical density: OD > 9 at 190–520 nm, OD > 7 at 520–532 nm, OD > 3 at 710–750 nm, OD > 5 at 750–850 nm, OD > 7 at 850–1080 nm and OD > 7 at 5000–11,000 nm).

4.2. Calibration procedure

To calibrate the new optical measurement technique, a reference measurement of the void fraction ε_{ref} is needed. As indicated above, the calibration set-up is used for this purpose and is equipped with a pressure transducer and a thermocouple (both calibrated inhouse). A micro-valve is also installed allowing for the introduction or removal of a precise quantity of the tested refrigerant mixed beforehand with rhodamineB. Each new quantity corresponds to a new reference void fraction. Considering the whole volume of the system (glass tube + circuit through pressure transducer and micro-valve), the void fraction of the system can be expressed as:

$$\varepsilon_T = \frac{\rho_L - \rho_T}{\rho_L - \rho_V} \tag{5}$$

where ρ_T is the density of the saturated mixture, ρ_L is the density of the saturated liquid phase and ρ_V is the density of the vapor. The saturation pressure measurement allows liquid and vapor densities ρ_L and ρ_V to be calculated and is used to estimate the saturated temperature, which is compared to the thermocouple measurement. A maximum difference of ±0.1 °C was observed over the total range of the reference void fraction measurements (from 0.05 to 0.95). This simple test confirms that the refrigerant vapor pressure curve does not change in presence of the fluorescent powder. Then, by measuring the total volume of the enclosure V_T and the mass of the refrigerant m_T using a gravimetric balance (Mettler Toledo model PR8002, accuracy of ±0.02 g), Eq. (5) can be rewritten to give the measured void fraction in terms of m_T and V_T:

$$\varepsilon_T = \frac{\rho_L - \frac{m_T}{V_T}}{\rho_L - \rho_V} \tag{6}$$

The total volume V_T is determined by completely filling the internal volume of the calibration set-up with water (after having pulled a high vacuum), and then measuring the temperature of the water (to accurately determine its density) and its mass. The optical measurement of the void fraction concerns only the level of liquid in the horizontal glass tube. Thus, with respect to the glass tube, the measured static void fraction ε_{ref} is given as

$$\varepsilon_{ref} = 1 - \frac{\rho_L - \frac{m_T}{V_T}}{\rho_L - \rho_V} \cdot \frac{V_T}{V} \tag{7}$$

where V is the internal volume of the glass tube. At each void fraction value, a series of 8–10 images of the illuminated cross-section is acquired. The aim is not to take several images of the

same state but to vary the laser beam intensity level in order to artificially take into account the changes in concentration of rhodamineB in the flow boiling test facility at the static state (that is to emulate range of concentrations confronted in dynamic conditions and corresponding levels of contrast at the interface).

The resulting images are in color and the chosen encoding system is the DSH system (density, saturation and Hue) also called HSL (Hue, saturation and luminance). The interest of such a transformation is in the simple and intuitive interpretation of the intensity values D and the two variables of chrominance S and H. Considering the present situation, the use of an optical filter to eliminate the light reflections from the tube walls and from the free surface results in images where the principal colour is orange. The extraction of the luminance plane yields a sharp contrast between the vapor zone and the liquid zone. Concentrating only in the liquid zone, the luminance component is more sensitive to the laser intensity than the red component in the RGB system. However, the contrast between the liquid and vapor zone is not represented by a discontinuous function of the luminance. A typical evolution of a luminance signal is represented in Fig. 11, with information extracted from the median pixel column of a transformed image corresponding to a void fraction of 55% and a laser intensity level of 61%. The transition from the gas zone in which the luminance L is on the order of 50 bits to the liquid zone where $L \cong 200$ bits occurs over 10–15 pixels. It is necessary to fix a luminance threshold above which a gas phase is considered present, and inversely, below which there is a liquid phase. In terms of image processing, selecting only one pixel with a luminance above the threshold is sufficient to consider all the contiguous pixels also with a luminance above the threshold as belonging to the liquid cross-sectional area (this corresponds to the well known function called *magic wand*). Thus the upper border of this zone represents the liquid–vapor interface. Selecting all the pixels above this limit but inside the mask, we obtain the representative surface of the vapor phase. Finally, dividing the number of pixels, which represents this vapor phase with the total number of pixels that are inside the mask, one finds the void fraction. Thus, for each luminance threshold selected (e.g., in the current image shown the luminance threshold ranges from about 50 to 200) there corresponds a unique void fraction value. In fact, changing the luminance threshold controls the height of the interface. Similarly, the extremities of the interface can be used to determine the dry angle around the perimeter of the tube.

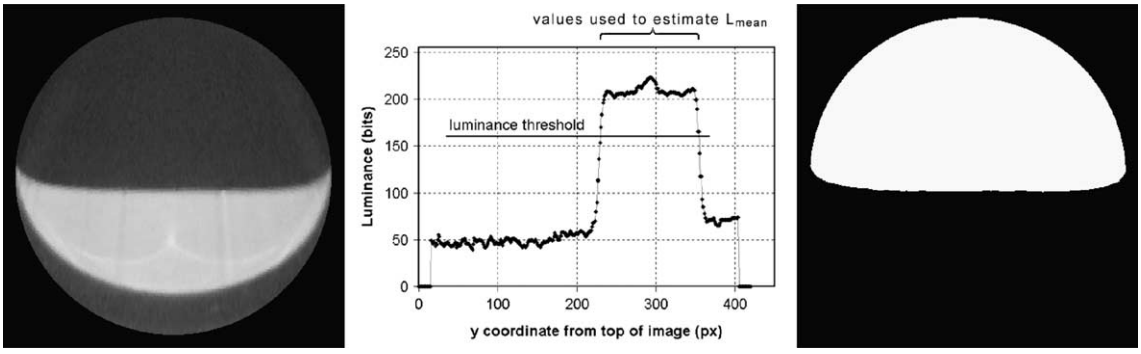

Fig. 11. Transformed image (luminance plane) of the illuminated cross-section (left), luminance intensity over the median vertical line (center) and extracted vapor zone corresponding to a fixed threshold value (right).

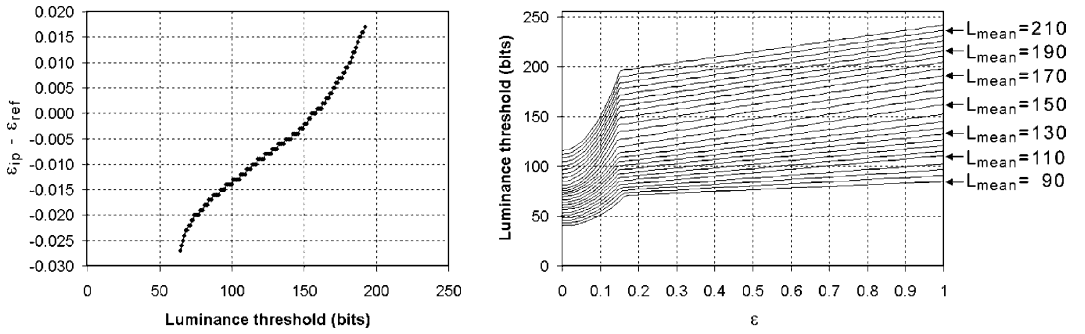

Fig. 12. Void fraction error in function of the luminance threshold (left) and calibration diagram (right).

On this basis, considering the reference void fraction as being an exact value, one can study the evolution of the void fraction measured by image processing ε_{ip} as a function of the luminance threshold. Thus the luminance threshold to impose on an image is the one that will give ε_{ip} equal to ε_{ref} (Fig. 12, on the left). This diagram shows a possible variation in void fraction from −0.027 to +0.017 as a function of the luminance threshold would be found if no calibration procedure was used. However, the image processing program must be able to determine the void fraction, no matter the intensity of the image (i.e. the intensity of the liquid phase on the image). To distinguish two images in which the void fraction is identical but where the luminance level is different, the program measures the mean luminance L_{mean} over the liquid phase area for a given threshold (i.e. over all contiguous pixels with a luminance value higher than the threshold). Therefore, the calibration technique consists of determining the luminance threshold as a function of both the reference void fraction and the mean luminance over the liquid zone (Fig. 12, on the right). This is the calibration diagram. During the process, the search of the optimum luminance threshold is determined iteratively. An initial threshold (on the order of 80 bits) allows a first estimation of void fraction and mean luminance. These two parameters are introduced again into the calibration diagram from which a new threshold is taken. A third iteration is necessary and sufficient to achieve a good estimation of the void fraction (see Section 5). Generally, a fourth iteration only increases processing time without bringing a significant improvement to the measurement.

5. Verification of the measurement technique

To obtain a realistic estimate of the measurement errors involved in applying this technique to dynamic conditions, it has been compared to static void fraction measurements over nearly the entire range. Thus, static calibration images are introduced into the image processing program and analyzed. The differences between ε_{ip} and ε_{ref} are determined and shown on the Fig. 13 (on the left). Consequently, the maximum difference between the measured void fraction and the reference void fraction is ±0.004. Statistically, the distribution of the measured errors is slightly biased towards negative values; however, this is not systematically the case. For certain void fractions, the mean error is positive (e.g., for $\varepsilon_{ref} = 0.05$ or $\varepsilon_{ref} = 0.40$).

It must also be mentioned that the reference void fraction also has a certain measurement error, $\Delta\varepsilon_{ref}$. As shown in Eq. (7), ε_{ref} depends on five parameters, which are measured experimentally,

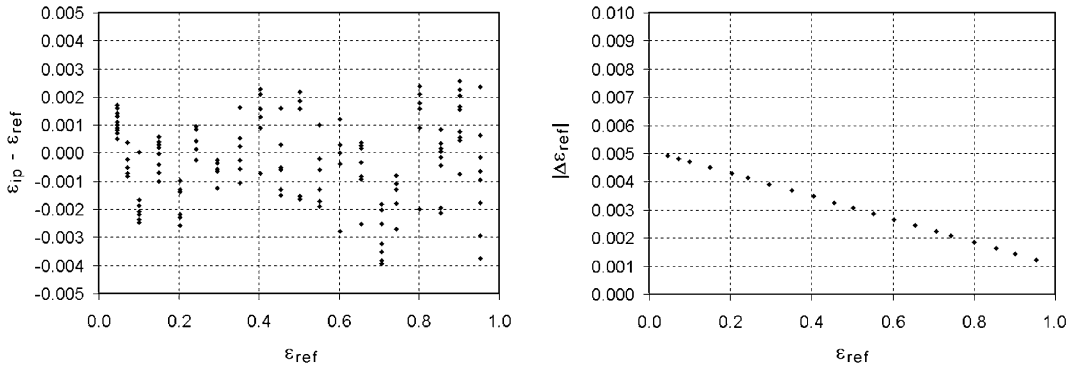

Fig. 13. Error measurements on calibration images (on the left) and error measurement on ε_{ref} (on the right).

and two of which depend on the pressure (the saturated vapor density and the saturated liquid density of the refrigerant). Considering these parameters to be linearly independent, an error calculation shows that $\Delta\varepsilon_{ref}$ does not exceed in its absolute value 0.005 for $\varepsilon_{ref} = 0.05$ and that $\Delta\varepsilon_{ref}$ tends to 0.001 for $\varepsilon_{ref} = 0.95$ (Fig. 13, on the right).

In summary, defining $\Delta\varepsilon_{ip}$ as the error of the void fraction measured by image processing, it can be said that in the worst case the void fraction measurement error of this new optical technique can be estimated to be $\Delta\varepsilon = \Delta\varepsilon_{ref} + \Delta\varepsilon_{ip}$ and is on the order of ± 0.01 over the entire range of void fractions measurable ($0.05 < \varepsilon < 0.95$).

6. Dynamic dry angle measurements

Figs. 14 and 15 present the experimental values of dry angle obtained from processing the videos. The dry angles shown are time-averaged values. The values are accurate to about $\pm 10°$, except at high vapor qualities ($x > 0.75$) where the two ends of the thin liquid arc remaining cannot be detected accurately. The maximum feasible dry angle can be predicted by assuming a completely stratified flow and using a void fraction equation (i.e. Eq. (4) in part II) to determine θ_{dry}. As can be seen, most of the measured values are equal to or less than this maximum value, and are quite well represented by this simple prediction. In Fig. 15(d), annular flow as encountered at $x = 0.52$ and hence no data for $x > 0.52$ are measurable using our technique. The measured values for $x > 0.75$ tend to fall off in value at high vapor qualities because of limitations in the measurement technique as noted above, and these values are thus only approximate indications of their real values ($\pm 30°$).

Also shown in Figs. 14 and 15 is a comparison to the dry angle prediction method proposed by Hart et al. (1989). This method is only applicable at high liquid holdups and is seen to give much lower values than observed here. Even with our measurement limitations at high vapor qualities as noted above, visual observations show that they were certainly not as low as their predictions shown in Fig. 14(c) and (d) and 15(b) and (c). This illustrates the significant difference between refrigerants and water in such flows and demonstrates why air–water flows are not representative of most working fluids, which have much smaller surface tension and contact angles.

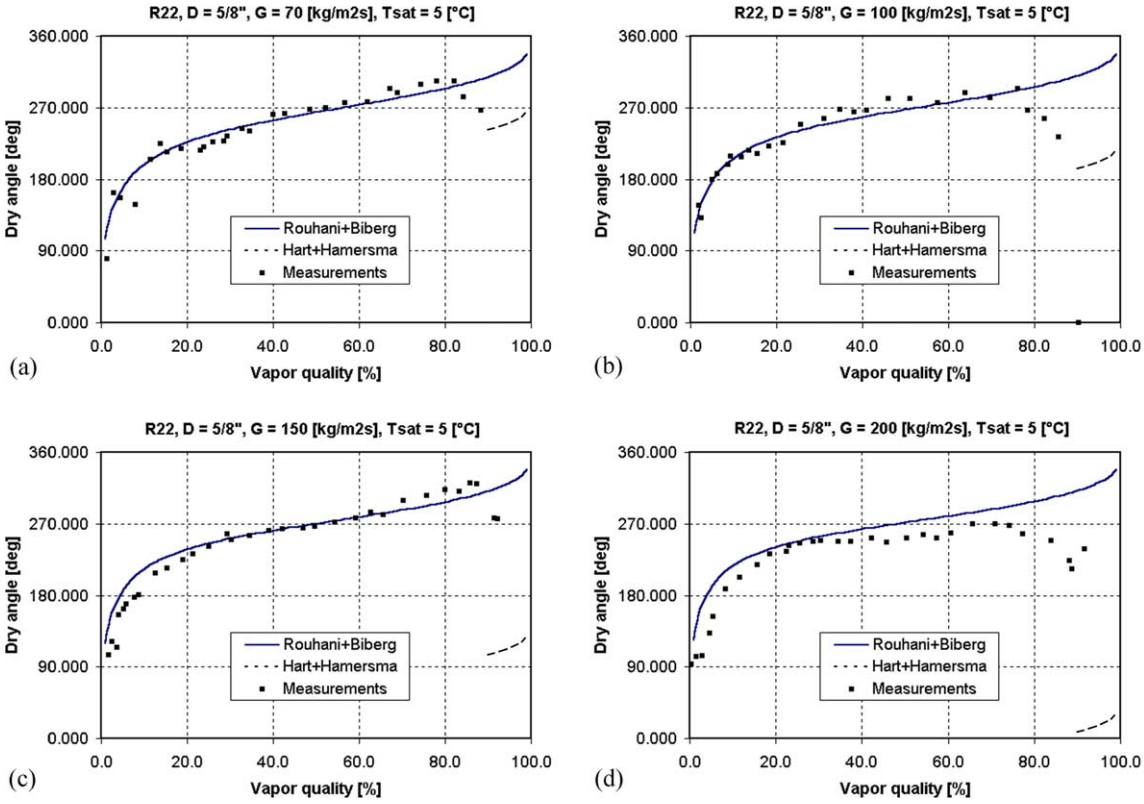

Fig. 14. Evolution of the dry angle as a function of vapor quality for R-22 at four mass velocities: (a) 70, (b) 100, (c) 150 and (d) 200 kg/m^{2}s.

7. Conclusions

A new optical measurement technique to dynamically measure the location of the vapor–liquid interface in two-phase stratified flows in horizontal tubes has been proposed, with a description of the practical and theoretical approach of the method, from the realization of an experimental set-up to the image analysis system. This work was developed in parallel with measurements of flow boiling heat transfer coefficients for two refrigerants (R-22 and R-410A). The new method is non-intrusive and allows measurements of the dry angle and void fraction through a glass tube in a cross-sectional view perpendicular to the flow. It is based on the recording of images of the bi-phasic fluid illuminated by a laser sheet. With an image processing program, it is possible to compensate for the distortion of the vision area (due to the presence of the tube glass wall) and to reconstruct an orthogonal, non-distorted view of the illuminated section. This reconstruction was developed based on a simulation of the deformation area of the acquired images. The use of a trace concentration of a fluorescent powder in the refrigerant to highlight the interface allows the image processing system to accurately delineate the interface vapor–liquid of the refrigerant in order to extract the dry angle and cross-sectional void fraction. This technique has been optimized for stratified types of flow and some slug flows, all without entrained bubbles, and yields void

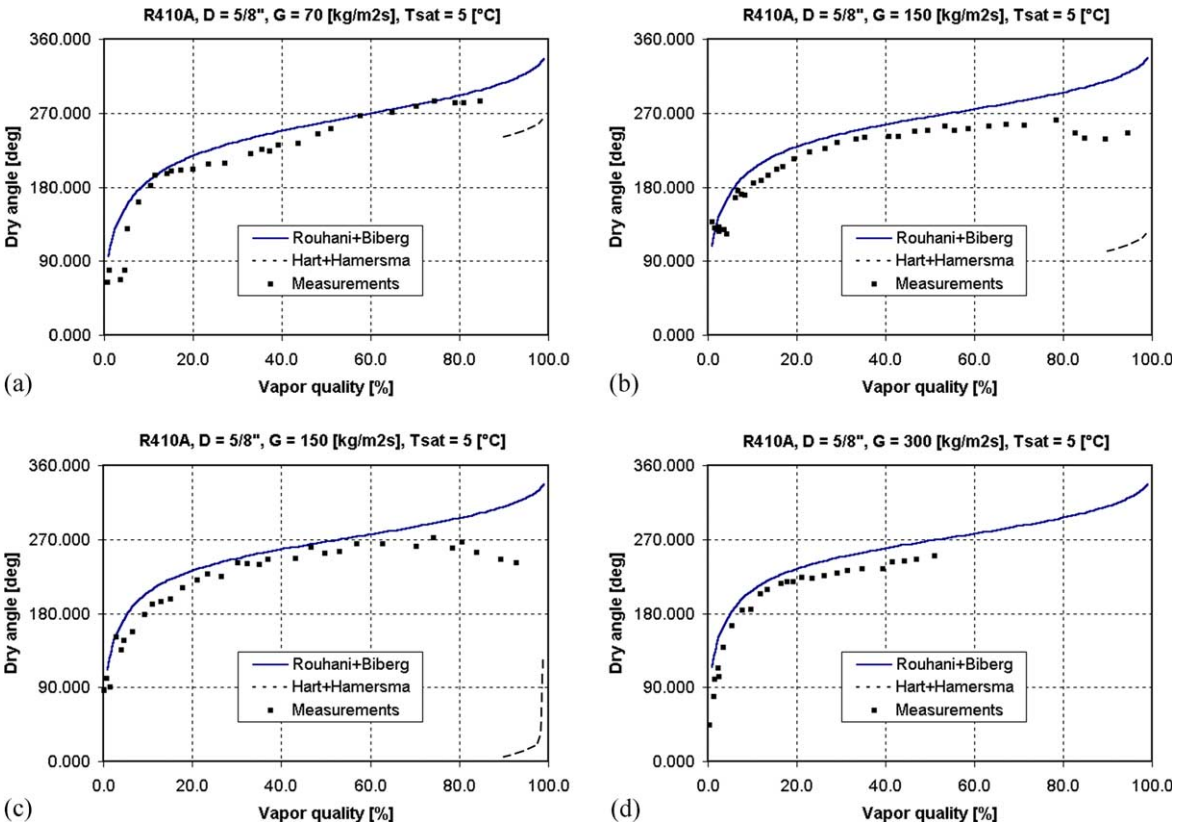

Fig. 15. Evolution of the dry angle as a function of vapor quality for R-410A at four mass velocities: (a) 70, (b) 150, (c) 200 and (d) 300 kg/m^{2}s.

fractions with a measured precision in absolute value on the order of ±0.01 over the range from 0.05 to 0.95. Dry angles are also reported and are accurate to about ±10°.

Acknowledgements

This investigation was supported by the Swiss National Science Foundation (FNS) contract number 21-57210.99 and by the Air-Conditioning and Refrigeration Technology Institute (ARTI) contract number 605-20040.

References

Cartellier, A., 1996. Measurements of gas phase characteristics using new monofiber optical probes and real-time signal processing. Nucl. Eng. Design 184, 393–408.

Costigan, G., Whalley, P.B., 1996. Slug flow regime identification from dynamic void fraction measurements in vertical air–water flows. Int. J. Multiphase Flow 23, 263–282.

Hart, J., Hamersma, P.J., Fortuin, J.M.H., 1989. Correlations predicting frictional pressure drop and liquid holdup during horizontal gas–liquid pipe flow with a small liquid holdup. Int. J. Multiphase Flow 15, 947–964.

Harvel, G.D., Hori, K., Kawanishi, K., Chang, J.S., 1999. Cross-sectional void fraction distribution measurements in a vertical annulus two-phase flow by high speed X-ray computed tomography and real-time neutron radiography techniques. Flow Measure. Instrum. 10, 259–266.

Huang, H.T., Fiedler, H.E., Wang, J.J., 1993. Limitation and improvement of PIV: part II: particle image distortion, a novel technique. Exp. Fluids 15, 263–273.

Kattan, N., Thome, J.R., Favrat, D., 1998a. Flow boiling in horizontal tubes: Part 1—Development of a diabatic two-phase flow pattern map. J. Heat Transfer 120, 140–147.

Kattan, N., Thome, J.R., Favrat, D., 1998b. Flow boiling in horizontal tubes: Part 2—New heat transfer data for five refrigerants. J. Heat Transfer 120, 148–155.

Kattan, N., Thome, J.R., Favrat, D., 1998c. Flow boiling in horizontal tubes: Part 3—Development of a new heat transfer model based on the flow pattern. J. Heat Transfer 120, 156–165.

Kendoush, A.A., Sarkis, Z.A., 2002. Void fraction measurement by X-ray absorption. Exp. Therm. Fluid Sci. 25, 615–621.

Krepper, E., Krussenberg, A.-K., Prasser, H.-M., Schaffrath A., 1999. High resolution void fraction measurements for the validation of flow maps and CFD codes. Two-phase Flow Modelling and Experimentation, Edizioni ETS, Pisa, pp. 1371–1378.

Thome, J.R., El Hajal, J., Cavallini, A., 2003. Condensation in horizontal tubes, part 2: new heat transfer model based on flow regimes. Int. J. Heat Mass Transfer 46, 3365–3387.

Westerweel, J., 1997. Fundamentals of digital particle image velocimetry. Meas. Sci. Technol. 8, 1379–1392.

Xu, L.J., Xu, L.A., 1997. Gas/liquid two-phase flow regime identification by ultrasonic tomography. Flow Meas. Instrum. 8, 145–155.